

Influence of ENSO on Pacific Decadal Variability: An Analysis Based on the NCEP Climate Forecast System

HUI WANG

Climate Prediction Center, NCEP/NWS/NOAA, Camp Springs, Maryland, and Wyle Science, Technology and Engineering Group, McLean, Virginia

ARUN KUMAR, WANQIU WANG, AND YAN XUE

Climate Prediction Center, NCEP/NWS/NOAA, Camp Springs, Maryland

(Manuscript received 4 October 2011, in final form 22 February 2012)

ABSTRACT

The influence of El Niño–Southern Oscillation (ENSO) on Pacific decadal variability (PDV) is investigated by comparing two 500-yr simulations with the National Centers for Environmental Prediction (NCEP) Climate Forecast System coupled model. One simulation is a no-ENSO run, in which model daily sea surface temperature (SST) in the tropical Pacific Ocean is relaxed to the observed climatology. The other simulation is a fully coupled run and retains ENSO variability. The PDV considered in this study is the first two empirical orthogonal functions of monthly SST anomalies in the North Pacific: the Pacific decadal oscillation (PDO) and the North Pacific Gyre Oscillation (NPGO). The PDO in the no-ENSO run can be clearly identified. Without ENSO, the PDO displays relatively higher variance at the decadal time scale and no spectral peak at the interannual time scale. In the ENSO run, the PDO variability increases slightly. ENSO not only enhances the variability of the PDO at the interannual time scale, but also shifts the PDO to longer time scales—both consistent with observations. ENSO modulates the Aleutian low and associated surface wind over the North Pacific. The latter, in turn, helps establish a more persistent PDO in the ENSO run. The results also indicate a PDO modulation of global ENSO impacts and the linearity in the superposition of the ENSO-forced and PDO-related atmospheric anomalies. Compared to observations, the NPGO in both simulations lacks power at the time scale longer than 30 yr. On the decadal time scale, the variability of the NPGO is weaker in the ENSO run than in the no-ENSO run.

1. Introduction

Pacific decadal variability (PDV) is dominated by the Pacific decadal oscillation (PDO; Mantua et al. 1997; Zhang et al. 1997), which is represented by the leading empirical orthogonal function (EOF) of monthly mean sea surface temperature (SST) anomalies in the North Pacific Ocean. Some studies have indicated that the PDO is not a single physical mode, but rather the result of several mechanisms (e.g., Schneider and Cornuelle 2005; Liu 2012). They include both tropical forcing associated with El Niño–Southern Oscillation (ENSO) and extratropical atmospheric stochastic forcing, as well as oceanic processes, such as changes in North Pacific

oceanic gyre and Kuroshio Extension and the re-emergence of SST anomalies due to the strong seasonal cycle of oceanic mixed layer depth (e.g., Latif and Barnett 1994; Alexander et al. 1999; Qiu 2003; Wu et al. 2003; Yeh and Kirtman 2005; Taguchi et al. 2007; Chhak et al. 2009).

Some studies have shown that the observed variability of the PDO can be reproduced using a first-order autoregressive model forced by the variability of ENSO and some of the above-mentioned processes (Newman et al. 2003; Schneider and Cornuelle 2005; Shakun and Shaman 2009). It is suggested that ENSO contributes significantly to the PDO variance at both interannual and decadal time scales (Schneider and Cornuelle 2005). An observational study (An et al. 2007) also hypothesized that the asymmetry in the extratropical response to El Niño and La Niña can generate the PDO accounting for significant amount of the PDO variance.

Corresponding author address: Dr. Hui Wang, NOAA Climate Prediction Center, 5200 Auth Road, Camp Springs, MD 20746.
E-mail: hui.wang@noaa.gov

In contrast, the influence of PDO on tropical SST variability was found to be relatively weak in a recent modeling study (Deser et al. 2012).

Although the PDO can be viewed as a reddened response to ENSO (Newman et al. 2003; Shakun and Shaman 2009), the net effects of ENSO on the PDO have not been clearly described or documented. The difficulty of assessing such effects rises from the facts that the PDO results from multiple mechanisms and the influence of ENSO on the PDO cannot be separated from the observational data alone or from coupled model simulations that contain both ENSO and PDO variability.

The purpose of this study is to explore (i) the characteristics of the PDO in the absence of tropical ENSO variability and (ii) the influence of ENSO on PDV through a comparison of two 500-yr coupled model simulations with and without ENSO SST variability. PDV in this study refers to the variability of North Pacific SST depicted by the first two leading EOFs. One is the PDO, and the other is the North Pacific Gyre Oscillation (NPGO; Di Lorenzo et al. 2008). The latter was originally defined as the second EOF of sea surface height anomalies in the North Pacific (Di Lorenzo et al. 2008), but it can also be captured by the second EOF of the North Pacific SST anomalies in the observations. Similar to the PDO, the NPGO is characterized by the basin-scale features associated with the decadal variations of North Pacific Ocean current and the Kuroshio Extension (Ceballos et al. 2009; Di Lorenzo et al. 2009).

In this study the nature of PDV without the influence of ENSO is examined first. This is achieved in a coupled model simulation through the relaxation of daily model predicted SST in the tropical Pacific to the climatological seasonal cycle of daily SST derived from observations. SSTs in the rest of the global oceans remain freely coupled with the atmosphere. In this way, the variability of the tropical Pacific SST, which is dominated by ENSO, is removed from the 500-yr model integration. In this no-ENSO run, processes other than ENSO (e.g., atmospheric stochastic forcing) are responsible for PDV generated in the model. The experiment is similar to one of the simulations reported in Wu et al. (2003) and Wu and Liu (2003), in which global tropical SSTs between 20°S and 20°N in a coupled model were replaced with the climatological annual cycle of SST.

The second 500-yr simulation is a fully coupled run. PDV in this coupled run results from both the ENSO-induced variability and mechanisms as those in the no-ENSO run. The differences in the characteristics of PDV between the ENSO run and no-ENSO run are interpreted as the influence of ENSO, and could be both linear and nonlinear in their characteristics.

Among the questions we investigate in this study are the following: What are the characteristics of PDV without the ENSO influence? What are the differences in intensity and frequency of PDV between the no-ENSO run and ENSO run? How does ENSO affect the atmospheric forcing for PDV? How are the ENSO-related atmospheric anomalies modulated by the PDO?

This paper is organized as follows. Section 2 provides a brief description of the model and experimental design. The characteristics of PDV without ENSO forcing are examined in section 3. Section 4 analyzes PDV with the ENSO variability. Comparisons between the two 500-yr runs for the atmospheric circulation and ocean temperature anomalies related to PDV are presented in section 5. Conclusions are given in section 6.

2. Model and experiments

The model used is the National Centers for Environmental Prediction (NCEP) Climate Forecast System (CFS) coupled model, version 1 (Saha et al. 2006). The CFS has been the operational seasonal forecast system at NCEP since 2004. The atmospheric, oceanic, and land components of the CFS are the NCEP Global Forecast System (GFS), version 1 (Moorthi et al. 2001), the Geophysical Fluid Dynamics Laboratory (GFDL) Modular Ocean Model, version 3 (MOM3; Pacanowski and Griffies 1998), and the Oregon State University (OSU) land surface model (LSM; Pan and Mahrt 1987), respectively.

In this version of the CFS, the atmospheric GFS has a horizontal resolution of T62 and 64 vertical levels. The GFDL MOM3 covers global oceans from 74°S to 64°N, with horizontal resolutions of 1° (longitude) by 1/3° (latitude) between 10°S and 10°N, and increasing to 1° (latitude) poleward of 30°S and 30°N. The ocean model has 40 layers from 5 m below sea level to 4479 m, with a 10-m resolution in the upper 240 m. The OSU LSM has two soil layers: 0–10 cm and 10–190 cm. More detailed descriptions of the CFS can be found in Saha et al. (2006).

The CFS has demonstrated skillful seasonal forecasts for a number of important climate systems, including ENSO (Wang et al. 2005; Zhang et al. 2007), the Asian–Australian monsoon (Wang et al. 2008), and the North American monsoon (Yang et al. 2009). The CFS also provides large-scale atmospheric and oceanic conditions for making statistical seasonal forecasts of Atlantic hurricanes (Wang et al. 2009; Vecchi et al. 2011). An overview of CFS version-1 performance is given in Saha et al. (2006) and Wang et al. (2010).

In the no-ENSO simulation, the ENSO SST variability is removed by assimilating the daily SST climatology into the CFS in the tropical Pacific (10°S–10°N, 140°E–75°W). This is done by replacing the model predicted SST in this region with new SST (SST_{new}) after one day of coupled model integration, which is a combination of the model SST predicted by the MOM3 (SST_{MOM3}) and observed daily SST climatology (SST_{OBS}) based on the following equation:

$$SST_{\text{new}} = (1 - w)SST_{\text{MOM3}} + wSST_{\text{OBS}},$$

where w is a weighting coefficient, and is set to $1/3$ in the tropical Pacific domain (10°S–10°N, 140°E–75°W) and is linearly reduced to 0 on the border of an extended domain (15°S–15°N, 130°E–65°W). The observed daily SST climatology is interpolated from long-term mean monthly SST derived from the National Oceanic and Atmospheric Administration (NOAA) Optimum Interpolation SST (OISST) V2 (Reynolds et al. 2002) over the 1981–2008 period. The use of SST_{OBS} with $w = 1/3$ is equivalent to relaxing the model-produced SST to the observed climatology at an e -folding time of 3.3 days, which effectively removes interannual variability in the tropical Pacific.

The second simulation—the ENSO run—is a free simulation that allows full air–sea interaction over the global oceans including the tropical Pacific. Both the no-ENSO and ENSO runs were integrated for 500 yr from the same initial conditions of 1 January 1981, obtained from the NCEP–Department of Energy (NCEP–DOE) Reanalysis 2 (R2; Kanamitsu et al. 2002) for the atmosphere and from the NCEP Global Ocean Data Assimilation System (GODAS; Behringer and Xue 2004) for the oceans.

The particular mode of PDV we are most interested in has a spatial pattern similar to the PDO, which is the leading EOF of observed monthly mean North Pacific SST anomalies (Mantua et al. 1997; Zhang et al. 1997), and is often associated with ENSO. As shown later, the second leading mode in the observations, the NPGO, is less influenced by ENSO. Prior to the EOF analysis, global mean SST anomaly is removed to suppress the influence of global mean SST, which is a procedure similar to that used by Mantua et al. (1997). The analysis of the 500-yr ENSO run suggests that the CFS can reproduce the major features of the observed ENSO variability (Kim et al. 2012) and the seasonality of the PDO (Wang et al. 2012). This provides confidence for assessing the ENSO influence on PDV with the CFS. A comparison between PDV in the ENSO run and no-ENSO run is expected to delineate the effect of ENSO on PDV.

PDV in the CFS simulations is also compared with observations. The observational dataset for SST is the NOAA Extended Reconstructed SST (ERSST) V3b (Smith et al. 2008). The ERSST is on a $2^\circ \times 2^\circ$ (latitude \times longitude) grid. The latest 100-yr monthly mean data (1911–2010) are used. The observed atmospheric wind fields are taken from the NCEP–National Center for Atmospheric Research (NCEP–NCAR) reanalysis (Kalnay et al. 1996) from 1948 to 2011 on a $2.5^\circ \times 2.5^\circ$ grid.

3. PDV in the no-ENSO run

PDV in this study is represented by the two leading EOFs of monthly mean North Pacific (20°–64°N, 125°E–100°W) SST anomalies (e.g., Furtado et al. 2011). Figure 1a shows the spatial pattern of SST anomalies associated with EOF1 of the North Pacific SST in the 500-yr no-ENSO run, obtained by regressing 500-yr monthly mean SST anomalies onto the principal component (PC) time series of EOF1. This mode accounts for 17% of North Pacific SST variance. The pattern correlation between this mode and the two leading EOFs in the ERSST (Figs. 1e and 1f) is 0.38 and 0.81, respectively, over the North Pacific. The latter two EOFs from the observations are the conventional PDO (Mantua et al. 1997) and NPGO (Di Lorenzo et al. 2008), and explain 24% and 12% of North Pacific SST variance, respectively. Thus, the spatial structure of SST in Fig. 1a is much closer to the NPGO (Fig. 1f) than the PDO (Fig. 1e), with cold SST anomalies to the south of 40°N in the central and western North Pacific and warm SST anomalies in a broad region to the north of 40°N and also in the eastern North Pacific.

The spatial pattern of SST associated with EOF2 in the no-ENSO run is shown in Fig. 1b. This mode accounts for 15% of North Pacific SST variance, which is close to EOF1. The pattern correlation between this mode and the PDO in the ERSST (Fig. 1e) is 0.79 and with the NPGO (Fig. 1f) is -0.33 . EOF2 in the no-ENSO run is thus closer to the PDO pattern in observations.

The relevance of the two EOFs (Figs. 1a,b) to the observed PDV (Figs. 1e,f) is also assessed by projecting the model SSTs onto the observed PDV patterns and then calculating the temporal correlation between the time series of the projection coefficients and the two PC time series of the model SSTs. Table 1 lists both the spatial pattern correlations and temporal correlations for the two leading EOFs. Consistent with the pattern correlations, the projection coefficients of the North Pacific SST from the no-ENSO run onto the observed PDO (NPGO) pattern are highly correlated with the PC time series of EOF2 (EOF1) of the model SSTs, with a correlation coefficient of 0.90 (0.90).

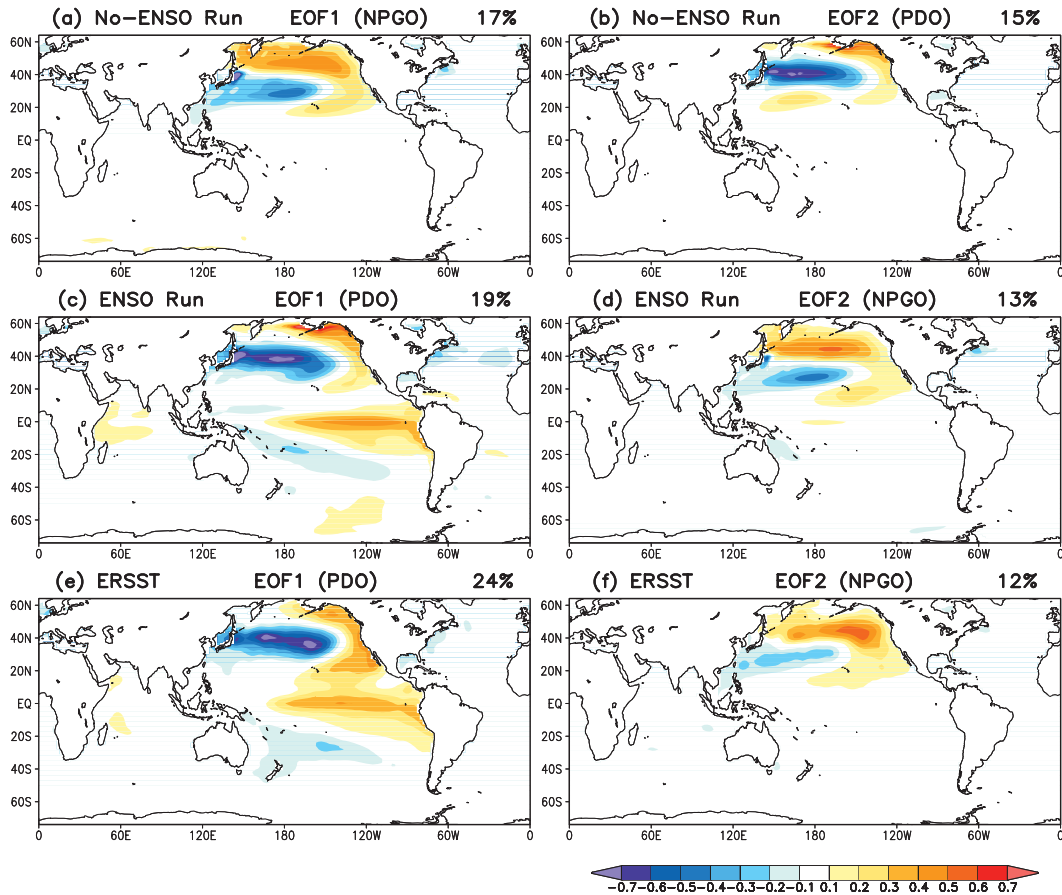


FIG. 1. Spatial pattern of SST anomalies (K) associated with (left) EOF1 and (right) EOF2 of monthly mean SST in the North Pacific (20°–64°N, 125°E–100°W) from the (a),(b) 500-yr no-ENSO run; (c),(d) 500-yr ENSO run; and (e),(f) 100-yr ERSST. The SST anomalies are obtained by regressing monthly mean SST anomalies onto the corresponding PC time series. The percentage of North Pacific SST variance explained by each mode is labeled at top right of each panel.

The power spectra of the PDO and NPGO in the no-ENSO run are shown in Fig. 2 (orange lines) together with those in the ERSST (black lines), obtained based on the analyses of the corresponding normalized PC time series. Each PC from the 500-yr model simulation is divided into five segments of 100 yr, which is comparable to the 100 yr in the ERSST. The power spectra shown in Fig. 2 for the CFS are an average of the spectra for the five segments. The statistical significance of spectral peaks is assessed by comparing these peaks to corresponding red-noise spectrum.

The PDO in the no-ENSO run is characterized by relatively strong power at the decadal time scale between 8 and 16 yr (Fig. 2a). In contrast, the PDO in the ERSST is dominated by both decadal and interannual variability, with two peaks at 33 and 5 yr. The NPGO in the no-ENSO run displays a wider range of spectra at the decadal time scale, ranging from 8 to 30 yr (Fig. 2b), while the NPGO in the ERSST is shifted toward lower

frequencies relative to the no-ENSO run. Compared to the observations, the peak frequencies of the two leading EOFs in the no-ENSO run are relatively high at the decadal time scale. The PDO lacks power at the interannual

TABLE 1. Spatial pattern correlations of the two leading EOFs of North Pacific SST in the ERSST (Figs. 1e,f) with those in the no-ENSO run and ENSO run (Figs. 1a–d), respectively. Values in parentheses are the temporal correlations between the two leading PC time series of the CFS SSTs and corresponding time series of projection coefficients of the model SSTs onto the observed PDO (Fig. 1e) and NPGO (Fig. 1f) patterns.

	No-ENSO run		ENSO run	
	EOF1 (NPGO)	EOF2 (PDO)	EOF1 (PDO)	EOF2 (NPGO)
ERSST				
EOF1 (PDO)	0.38 (0.36)	0.79 (0.90)	0.93 (0.99)	−0.02 (0.05)
EOF2 (NPGO)	0.81 (0.90)	−0.33 (−0.34)	0.04 (0.07)	0.88 (0.93)

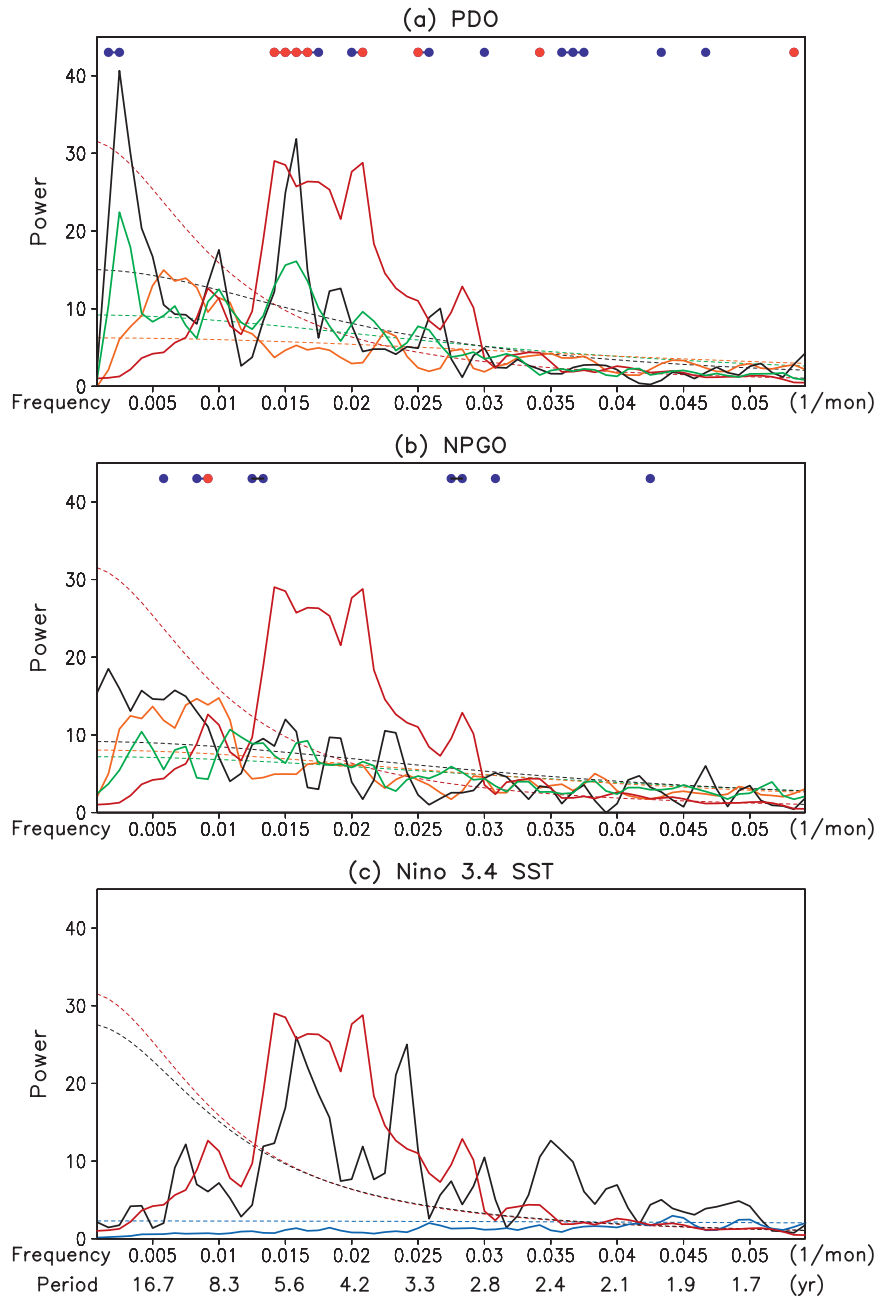


FIG. 2. Power spectra of the normalized PC time series for the (a) PDO and (b) NPGO in the no-ENSO run (orange), ENSO run (green), and ERSST (black); and (c) power spectra of normalized time series of Niño-3.4 SST in the no-ENSO run (blue), ENSO run (red), and ERSST (black). The power spectra for the CFS data are averages over five 100-yr segments. Dashed lines are corresponding red-noise spectra. Blue and red dots in (a) and (b) denote the frequency at which the difference in power between the no-ENSO run and ENSO run exceeds the 95% and 99% significance levels, respectively, based on a t test.

time scale presumably because of the lack of ENSO forcing in the simulation. An important result of the analysis of PDV variability in the no-ENSO run is that it contains variability similar to the PDO, and which could be modified by the ENSO variability in tropical Pacific.

4. PDV in the ENSO run

Figure 1c shows the spatial pattern of SST anomalies associated with EOF1 in the ENSO run. This mode resembles the observed PDO (Fig. 1e) with a pattern

correlation of 0.93 over the North Pacific and a temporal correlation of 0.99 (Table 1) between the PC time series of this mode and the projection coefficients of the model SST onto the observed PDO pattern. This mode accounts for 19% of North Pacific SST variance, which is slightly larger than the variance of 15% in the no-ENSO run, but is less than that in the observations (24%). A close inspection of Figs. 1b,c reveals that the elongated cold SST anomalies associated with the PDO pattern near 40°N in the no-ENSO run shifts somewhat toward south in the ENSO run. Warm SST anomalies are found near the date line between 20° and 30°N in the no-ENSO run (Fig. 1b) but not in the ENSO run (Fig. 1c). Similar to the observations (Fig. 1e), associated with the PDO, there are El Niño-like SST anomalies in the tropical Pacific (Fig. 1c), indicating the tropical–extratropical linkage. To summarize, in the presence of ENSO, the PDO becomes the first EOF and its variability is slightly enhanced.

The NPGO-like mode, as EOF2 in the ENSO run, is shown in Fig. 1d. The pattern correlation between this mode and the observed NPGO (Fig. 1f) is 0.88. The temporal correlation between the corresponding PC time series and the projection coefficients onto the observed NPGO is 0.93 (Table 1). The spatial structure of the NPGO in the ENSO run therefore more resembles the observed NPGO than in the no-ENSO run. The SST variance explained by the NPGO is 13% in the ENSO run, and is closer to the observations (12%).

The mean power spectra of the PDO and NPGO in the ENSO run are also shown in Fig. 2 (green lines), together with the power spectra of SST anomalies averaged in the Niño-3.4 region in the ENSO run (red line). The Niño-3.4 SST represents the variability of ENSO with high power at the interannual time scale, ranging from 4 to 6 yr in the CFS, and is comparable to the observations (Fig. 2c). The spectra averaged over the five 100-yr segments of the PDO in the ENSO run display two peaks at 33 and 5 yr, coincident with the PDO in the ERSST (Fig. 2a). The power of the two peaks, however, is much weaker than the observations. The results suggest that (i) ENSO increases the variability of the PDO at the interannual time scale, and (ii) it also shifts the PDO to a longer time scale (33 yr). The difference in frequency of the PDO between the ENSO run and no-ENSO run exceeds the 95% significance level at both the interannual and decadal time scales estimated based on a *t* test.

The inclusion of the ENSO variability in the ENSO run does not lead to a significant change in the frequency characteristics of the NPGO (Fig. 2b). A lack of interaction between ENSO and NPGO is consistent with

the finding of Furtado et al. (2011), who showed that the ability of coupled climate models to reproduce the observed NPGO is not as good as for the PDO. It is likely due to much weaker coupling between the NPGO and ENSO-related extratropical atmospheric circulation in the models, as suggested by Furtado et al. (2011), which leads to a relatively smaller influence of ENSO on the NPGO.

Unlike the observations, the NPGO in both the no-ENSO run and ENSO run lacks power at the time scale longer than 30 yr (Fig. 2b). A possible reason may be that NPGO variability is hypothesized to be influenced by SST variability in central Pacific (Di Lorenzo et al. 2010), which is found to be weaker in the CFS ENSO simulation (Kim et al. 2012). Additionally, on the decadal time scale, the variability of the NPGO is even weaker in the ENSO run than in the no-ENSO run, and reasons for this are not clear (as following the NPGO and central Pacific SST connection, a further reduction in central Pacific SST variability should have led to a smaller NPGO variance at lower frequencies). In the following analyses, we focus on the ENSO influence on the PDO.

5. PDO-related atmospheric circulation and ocean temperature anomalies

It is well recognized that ENSO affects the PDO via the atmospheric bridge mechanism (e.g., Alexander et al. 2002). ENSO modulates extratropical atmospheric circulation through teleconnection, which in turn affects local air–sea interaction and the PDO. To link the PDO to the extratropical atmospheric circulation, Figs. 3a and 3b show 1000-hPa wind and SST anomalies associated with the PDO in the no-ENSO run and ENSO run, respectively, based on linear regressions against the PC time series of the PDO. Anticipating that the PDO SST is a response to the surface wind forcing (e.g., Wang et al. 2012; also see Fig. 5), the regression patterns are shown for the wind anomalies leading the SST by one month.

The surface wind patterns in both the no-ENSO run and ENSO run are characterized by a basinwide cyclonic circulation over the North Pacific. The distribution of the surface wind is physically consistent with the SST anomalies (e.g., Wang et al. 2012) in that the surface wind forcing can lead to anomalous SSTs. Over the region of cold SST, there is northwesterly wind anomaly that will enhance the heat loss from the ocean because of the advection of the colder and drier air, and also generate advection of colder SST by Ekman transport (Chhak et al. 2009). Along the North American coast, southerly winds will induce on-shore Ekman

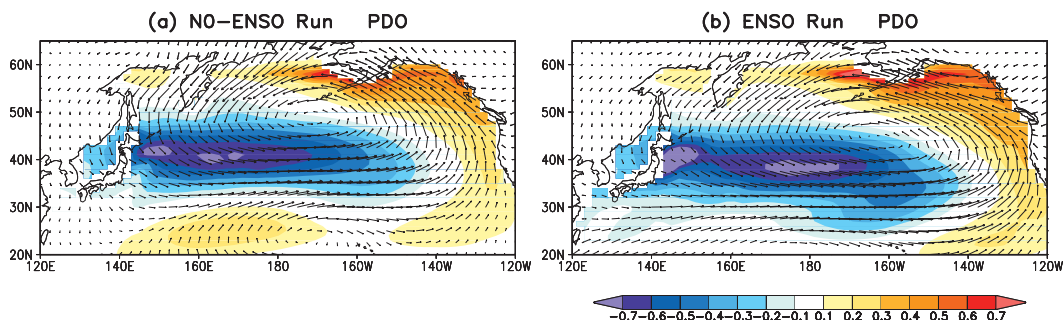


FIG. 3. Regression patterns of 1000-hPa wind (vectors; m s^{-1}) and SST (shadings; K) anomalies associated with one standard deviation departures of the PC time series of the PDO in the (a) no-ENSO run and (b) ENSO run. The wind anomalies lead the SST anomalies by one month.

transport and suppress coastal upwelling, which is consistent with the warm SST anomalies.

Some differences also exist in the surface wind pattern between Figs. 3a and 3b. The center of the cyclonic circulation in the no-ENSO run is shifted toward north as compared to that in the ENSO run, together with slightly northward shift of cold SST anomalies. In addition, an anticyclonic circulation is found in the lower latitudes between 20° and 30°N near the date line (Fig. 3a), where warm SST anomalies are located (Fig. 1b).

If the PDO is a consequence of the forcing from the overlying atmosphere, the PDO-related surface wind anomalies shown in Fig. 3 may also be related to the dominant modes of variability in the surface wind.

Figure 4 shows the 1000-hPa wind anomalies associated with the two leading EOFs of 1000-hPa zonal wind over the North Pacific in both the no-ENSO run and ENSO run. Both EOFs in the no-ENSO run (Figs. 4a and 4c) resemble their counterparts in the ENSO run (Figs. 4b and 4d), with a pattern correlation of 0.98 for both modes. The similarity in the EOF patterns indicates that ENSO variability has no significant impact on the spatial structure of these leading EOFs of the extratropical surface wind variability, which are likely determined by the modes of atmospheric internal variability.

EOF1 (Figs. 4a,b) is characterized by a basinwide cyclonic circulation, whereas EOF2 (Figs. 4c,d) is

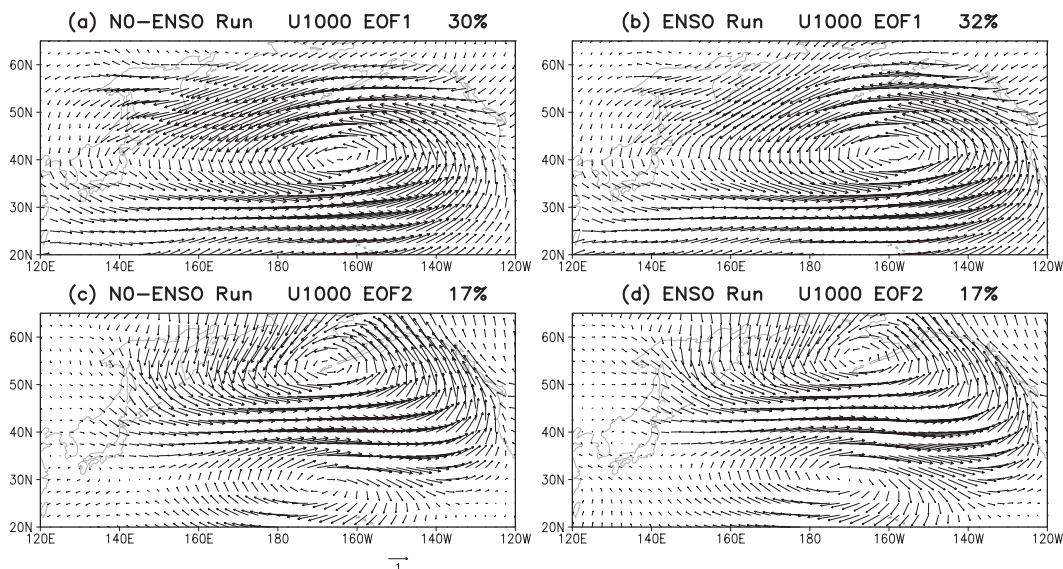


FIG. 4. Spatial pattern of 1000-hPa wind anomalies (m s^{-1}) associated with (a),(b) EOF1 and (c),(d) EOF2 of monthly mean 1000-hPa zonal wind over the North Pacific from the (left) no-ENSO run and (right) ENSO run. The anomalies are obtained by regressing 500-yr monthly mean zonal and meridional wind anomalies onto the corresponding PC time series. The percentage of 1000-hPa zonal wind variance explained by each mode is labeled at top right of each panel.

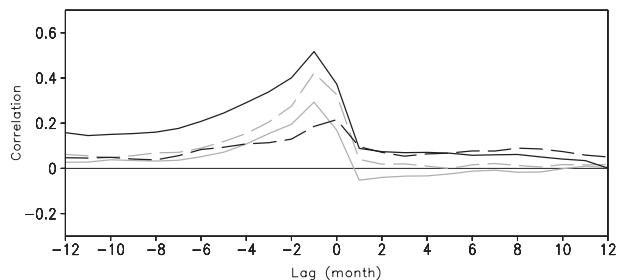


FIG. 5. Lag correlations between the 500-yr monthly PC time series of the PDO and two leading EOFs of 1000-hPa zonal wind in the no-ENSO run (gray) and ENSO run (black), respectively. Solid (dashed) lines denote the correlations between the PDO and EOF1 (EOF2) of the 1000-hPa zonal wind. Negative lag means the 1000-hPa zonal wind leading the SST.

characterized by a dipole with a center of cyclonic circulation to the north and anticyclonic to the south. The wind distributions of both EOFs are consistent with the sea level pressure patterns documented in Chhak et al. (2009) and Furtado et al. (2011) that were found to covary with the PDO and NPGO, respectively, with EOF1 closely related with the Aleutian low and EOF2 with the North Pacific Oscillation (NPO; Rogers 1981). The two modes account for 30% and 17% of the surface zonal wind variance, respectively, in the no-ENSO run and 32% and 17% in the ENSO run. The variance explained is consistent with observations (29% and 19%) in the NCEP-NCAR reanalysis (not shown).

The similarity of wind patterns between Figs. 3 and 4 is examined for both the no-ENSO run and ENSO run. The pattern correlations between the PDO-related zonal wind anomalies in Fig. 3 and the two EOFs of the 1000-hPa zonal wind in Fig. 4 are 0.53 and 0.80, respectively, in the no-ENSO run and 0.89 and 0.42 in the ENSO run. The higher correlation for the no-ENSO with EOF2 is due to northward shift in the PDO-related surface wind pattern (Fig. 3a). This implies that the PDO in the no-ENSO run (ENSO run) is more closely related to EOF2 (EOF1) of the surface zonal wind.

The PDO linkage to different atmospheric forcing between the two runs is also assessed based on lag correlations between monthly mean values of the PDO time series and the leading EOFs of the 1000-hPa zonal wind, as shown in Fig. 5. In general, significant correlations are found when the zonal wind leads the SST confirming the role of atmospheric variability as a forcing for the PDO. Correlations are weak when the zonal wind lags the SST.

In the no-ENSO run, the strongest correlation occurs when EOF2 of the zonal wind leads the PDO by one month. A relatively high correlation is also found when EOF1 of the zonal wind leads the PDO by one month.

This suggests that the PDO in the no-ENSO run is a combination of wind forcing associated with both EOF1 and EOF2, and is consistent with correlation between the spatial pattern of surface wind associated with the PDO (Fig. 3a) and the leading modes of surface wind variability in the no-ENSO run (Fig. 4, left panels) discussed above.

In the ENSO run, larger correlation is found when EOF1 of the surface zonal wind leads the PDO by one month, and the correlation is much higher than that for the no-ENSO run. The lag correlation between the PDO and EOF2 of the surface wind, on the other hand, becomes weaker. The results indicate that ENSO selectively enhances (reduces) the linkage of the PDO to the atmospheric forcing associated with EOF1 (EOF2) of the surface zonal wind. The Aleutian low is thus an important forcing for the PDO in the presence of ENSO.

Although ENSO has no apparent effect on the spatial pattern of the leading EOFs of the surface wind (Fig. 4), it may still affect their temporal characteristics. Figure 6 shows the power spectra of these EOFs in both runs and the Niño-3.4 SST in the ENSO run. In the no-ENSO run (Figs. 6a,b), the frequency distributions for both EOFs are characteristics of white noise and exhibit the stochastic nature of the extratropical atmospheric wind forcing, with no predominant peaks. In the ENSO run, there is an increase in the power at the interannual time scale in the power spectra of EOF1 (Fig. 6c), coincident with those of ENSO (Fig. 6e). The power spectrum of EOF2 basically remains the white noise (Fig. 6d). The results indicate that ENSO does modulate the interannual variability of the surface wind associated with the Aleutian low.

The effect of ENSO on the surface wind can also be seen in the autocorrelation of the corresponding PC time series, as shown in Fig. 7. The autocorrelation for EOF1 of the zonal wind in the ENSO run is higher than EOF2 in the ENSO run and is also higher than the two EOFs in the no-ENSO run at 1- to 4-month lag. The larger autocorrelation indicates more persistent atmospheric forcing associated with the Aleutian low for the North Pacific SST due to ENSO. This is to be expected as the slow ENSO variability in tropics, and its extratropical influence, will nudge the Aleutian low to be in a particular phase. Consequently, the PDO in the ENSO run will also tend to have a higher persistence than in the no-ENSO run. Further, the persistence of the PDO in ENSO run is closer to the observations, also shown in Fig. 7, and matches particularly well the PDO index of Mantua et al. (1997; available at <http://jisao.washington.edu/pdo/PDO.latest>).

It is interesting to note that when the ENSO-related variability is removed from the PC time series of the

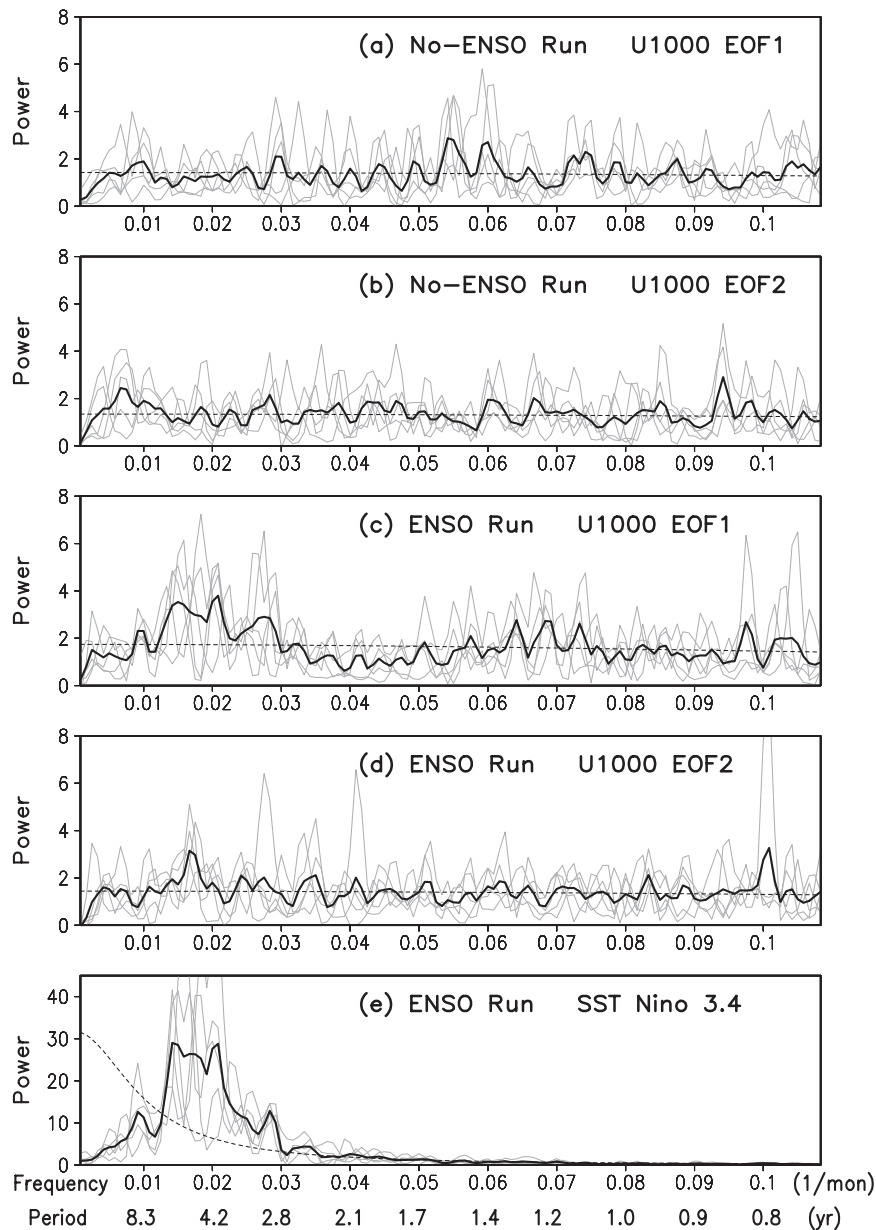


FIG. 6. Power spectra of the normalized PC time series of (a) EOF1 and (b) EOF2 of 1000-hPa zonal wind over the North Pacific in the no-ENSO run, corresponding (c) EOF1 and (d) EOF2 in the ENSO run, and (e) power spectra of the normalized time series of Niño-3.4 SST in the ENSO run. Gray lines are for five individual 100-yr segments. Black lines are averages over the five segments. Dashed lines are corresponding red-noise spectra.

PDO in the ENSO run, the PDO becomes much less persistent on seasonal time scale, and autocorrelation is closer to that in the no-ENSO run. Figure 7 provides a clear comparison between the model PDO and the observed PDO and shows how the seasonal variability in the PDO is changed in the no-ENSO run and also in the ENSO run when the ENSO-related variability is linearly removed.

The relative importance of the two EOFs of the surface zonal wind and ENSO to the PDO can be further estimated using a multiple linear regression model similar to that in Newman et al. (2003) and Shakun and Shaman (2009). Two sets of three predictors are used to reconstruct the $PC(t)$ time series of the PDO, including previous month $PC(t-1)$ values of the PDO and the two zonal wind modes in one set and previous month

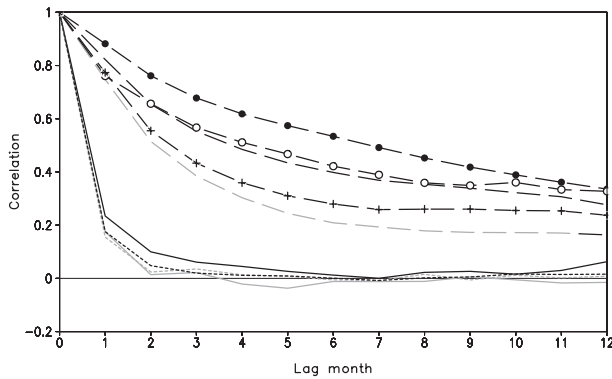


FIG. 7. Autocorrelations of the 500-yr monthly PC time series of EOF1 (solid lines) and EOF2 (short dashed lines) of 1000-hPa zonal wind over the North Pacific, the PDO (long dashed lines) in the no-ENSO run (gray) and ENSO run (black), the PDO in the ENSO run with the ENSO-related variability removed (long dashed black line with crosses), the PDO in the 100-yr ERSST (long dashed black line with dots), and the PDO index (long dashed black line with open circles; Mantua et al. 1997) for 1911–2010 (available at <http://jisao.washington.edu/pdo/PDO.latest>).

Niño-3.4 SST($t - 1$) instead of EOF2($t - 1$) of the zonal wind in another set. As shown later, EOF2($t - 1$) of the zonal wind has little contribution to the PDO(t) variability in the ENSO run and observations. The model is applied to the 500-yr no-ENSO run, ENSO runs, and 64-yr (1948–2011) ERSST with the NCEP–NCAR reanalysis data, respectively.

Cross-validated correlation skill R and percentage of variance P reproduced by the predicted PDO time series are listed in Table 2. The former is the correlation between the predicted PDO time series based on the three predictors and the PC time series of the PDO in the two runs and ERSST, respectively. The latter (i.e., P) is the percentage ratio of the variance of the predicted PDO time series to the variance of the corresponding PC time series of the PDO. To assess the contribution of each predictor to the variability of the PDO, the correlation between the PC time series of the PDO and the predicted counterpart associated with each predictor is calculated, and the percentage of variance contributed by each predictor is also estimated. This procedure is done by first evaluating the percentage of variance accounted for by the predicted PDO time series associated with PDO($t - 1$) only—the persistence of the PDO, which dominates the prediction of the PDO. Then the percentage of variance is reevaluated for the predicted PDO associated with both PDO($t - 1$) and one of the other two predictors. The increase in the percentage of variance due to adding one more predictor is taken as the contribution of that predictor. In this way, the variances explained by each predictor are approximately additive.

The correlation between the PC time series of the PDO and the predicted is 0.79, 0.85, and 0.90 for the no-ENSO run, ENSO run, and observations, respectively, with 62%, 73%, and 81% of total variance explained by the predicted PDO time series. Most of the skill comes from the persistence of the PDO, which represents 42% of the total variance in the no-ENSO run, about 50% in the ENSO run, and 60%–70% in the observations. The higher skill for the observations is consistent with the higher persistence of the PDO in the ERSST (Fig. 7). Adding other predictors does not improve the forecast skill much, but increases the variance of the predicted time series by 10%–20%. For example, the forecast skill for the PDO is 0.82 and 0.89 in the ENSO run and observations, respectively, based on the persistence of the PDO only. Including EOF1 of the zonal wind and the Niño-3.4 SST as predictors only increases the skill from 0.82 to 0.86 for the ENSO run and from 0.89 to 0.90 for the observations. However, increase in the percentage of variance explained is much larger and changes from 49% to 73% for the ENSO run and from 62% to 81% for the observations. This indicates the role of the surface wind and ENSO in enhancing the PDO variability.

Consistent with the results in Figs. 3–5, both EOF1 and EOF2 of the zonal wind are of predictive value for the PDO in the no-ENSO run, with EOF2 ($R = 0.42$, $P = 13\%$) more important than EOF1 ($R = 0.29$, $P = 7\%$). In contrast, EOF2 is not an appropriate predictor for the PDO in the ENSO run ($R = 0.18$, $P = 1\%$) and observations ($R = -0.1$, $P = 0\%$). EOF1 of the zonal wind is more important to the prediction of the PDO in the ENSO run ($R = 0.52$, $P = \sim 18\%$ – 20%) and observations ($R = 0.45$, $P = \sim 11\%$ – 12%). The ENSO-related skill in the ENSO run ($R = 0.43$, $P = 6\%$) is comparable to that in the observations ($R = 0.51$, $P = 8\%$). The related variance is less than 10%, and once again indicates a weak influence of ENSO variability on the PDO.

It is noted that the variances explained with the two sets of predictors are identical in both the ENSO run (73%) and the observations (81%). This is just a coincidence due to truncation and they are in fact not exactly the same. When replacing EOF2 of the zonal wind with the Niño-3.4 SST as the third predictor, there is a slight decrease in the percentage of variance accounted for by the persistence of the PDO and EOF1 of the zonal wind in both the ENSO run and observations. This may be another indication of the influence of ENSO on the persistence of the PDO and the surface wind in the North Pacific. Given no virtual changes in the percentage of variance explained with the two sets of predictors, the influence of ENSO can be well represented by the persistence of PDO and EOF1 of the zonal wind in

TABLE 2. Cross-validated correlation skill for the PDO index with a multiple linear regression model. The skill (column 2) is measured by the correlation between the PC time series of the PDO and the predicted PDO time series based on three predictors. The correlations between the PDO index and that associated with each predictor are also listed (columns 3–6). The values in parentheses are the percentages of the total variances explained by the predicted PDO index and those contributed by each predictor.

	Skill	Predictor($t - 1$)			
		PDO	EOF1 _{U1000}	EOF2 _{U1000}	Niño-3.4
No-ENSO run	0.79 (62%)	0.75 (42%)	0.29 (7%)	0.42 (13%)	
ENSO run	0.85 (73%)	0.82 (52%)	0.52 (20%)	0.18 (1%)	
ENSO run	0.86 (73%)	0.82 (49%)	0.52 (18%)		0.43 (6%)
Observation	0.90 (81%)	0.89 (69%)	0.45 (12%)	−0.10 (0%)	
Observation	0.90 (81%)	0.89 (62%)	0.45 (11%)		0.51 (8%)

predicting the PDO, without using the Niño-3.4 SST as an additional predictor.

Change in the characteristics of the PDO in the presence of ENSO is also likely to influence the vertical structure of the PDO-related oceanic anomalies. Figure 8 shows the longitude–depth cross section of ocean temperature anomalies associated with the PDO along 38°N where cold SST anomalies have the largest amplitudes in both runs (Fig. 3). These anomalies are obtained by regressing 500-yr monthly mean ocean temperature anomalies onto the PC time series of the PDO for the no-ENSO run and ENSO run (Figs. 8a and

8b), respectively. The cold temperature anomalies are stronger and penetrate deeper in the ENSO run than in the no-ENSO run. Temperature anomalies colder than 0.4 K penetrate only to the depth of 50 m in the no-ENSO run (Fig. 8a). However, they reach as deep as 120 m in the ENSO run (Fig. 8b). As the PDO in the ENSO run is less persistent when the ENSO-related variability is removed (Fig. 7), the larger and deeper ocean temperature anomalies may be a consequence of more persistent atmospheric forcing. Additionally, the enhanced lower-frequency variability of the PDO in the ENSO run (Fig. 2a) may also contribute to this

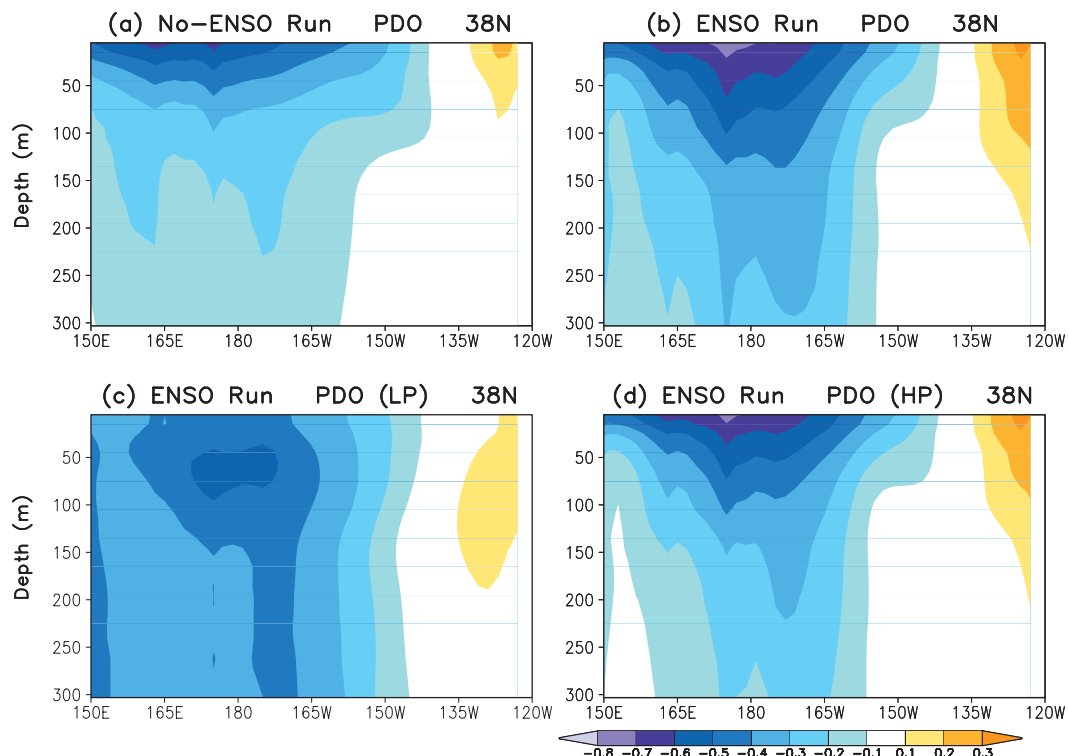


FIG. 8. Regression patterns of ocean temperature anomalies (K) along 38°N associated with one standard deviation departures of the PC time series of the PDO in the (a) no-ENSO run, (b) ENSO run, (c) ENSO run with the LP filtered (16 yr) PC time series, and (d) ENSO run with the HP filtered (16 yr) PC time series.

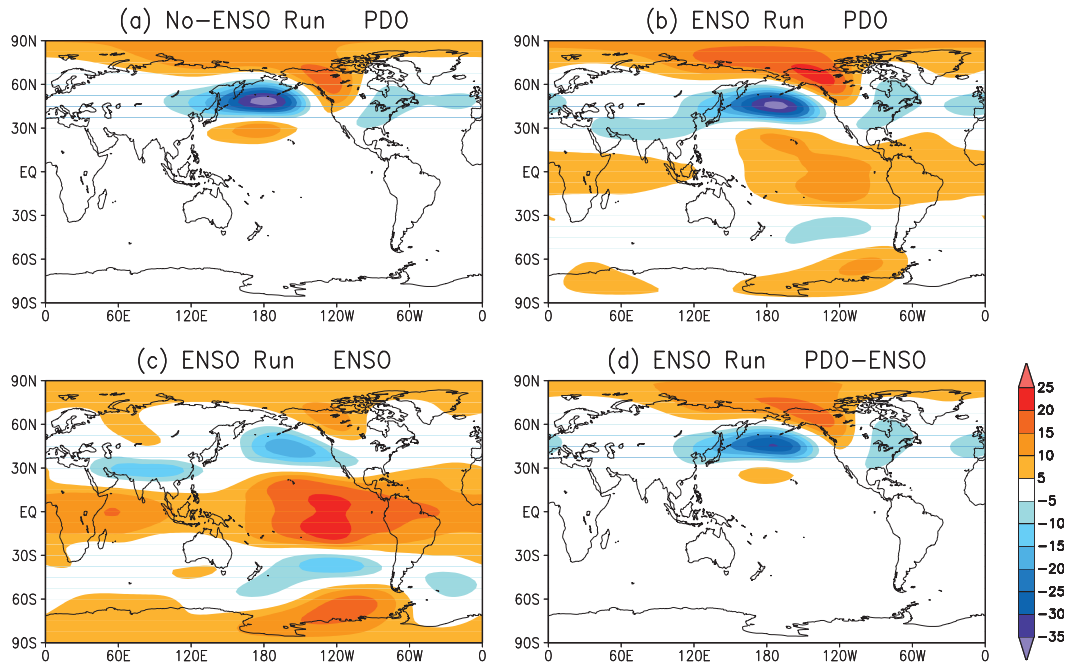


FIG. 9. Regression patterns of 200-hPa geopotential height anomalies (gpm) associated with one standard deviation departures of the PC time series of the PDO in the (a) no-ENSO run, (b) ENSO run, (c) associated with the time series of Niño-3.4 SST in the ENSO run, and (d) the PDO in the ENSO run after removing ENSO-related height anomalies.

deeper structure. To illustrate this possibility, the ocean temperature anomalies are regressed against the low-pass (LP) and high-pass (HP) filtered PDO PC time series with a cutoff period of 16 yr, respectively, shown in Figs. 8c and 8d. The deeper structure in the ENSO run is clearly attributed to the variability of the PDO at the time scale longer than 16 yr that is absent in the no-ENSO run (Fig. 2a). Why the ENSO run has PDO variability on these slow time scales remains to be investigated further.

We next compare the atmospheric and terrestrial anomalies associated with the PDO. Figure 9 shows 200-hPa geopotential height anomalies associated with the PDO in both runs as well as those associated with the ENSO variability in the ENSO run. In the no-ENSO run, the PDO-related height anomalies display a well-defined wave pattern over the Pacific–North American (PNA) region (Fig. 9a), and the anomalies are mainly confined to the extratropics. A similar wave pattern is also found in the ENSO run associated with the PDO (Fig. 9b) over the PNA region. Additionally, height anomalies are found in the tropics and the Southern Hemisphere, which is similar to the teleconnections associated with the Niño-3.4 ENSO SST (Fig. 9c; Wallace and Gutzler 1981). The height anomalies in Fig. 9b, therefore, contain a mix of variability associated with the PDO (Fig. 9b) and some impacts

from ENSO (Fig. 9c). After linearly removing the ENSO-related anomalies, the anomalous height field associated with the PDO in the ENSO run (Fig. 9d) does show the localized feature that is very similar to the no-ENSO run (Fig. 9a). A similar feature is also found with observational data (not shown). For the model simulations, the results also indicate a linear superposition of the remote ENSO influence and PDO-related anomalies. A comparison between Figs. 9c and 9d indicates that for the appropriate phase of ENSO and the PDO, the height anomalies can be twice as strong as those associated with ENSO alone over the PNA region. On the other hand, the extratropical influence of ENSO over the PNA region can also be diminished if the PDO is in a different phase.

Similar composites for precipitation anomalies over land are shown in Fig. 10. In the no-ENSO run, the fingerprints of the PDO are found in global monsoon regions (Fig. 10a). Associated with a positive phase of the PDO (Fig. 3a), South and North American monsoon precipitation tends to be above normal, whereas Asian and Australian monsoon precipitation tends to be below normal. Overall, the PDO-related precipitation anomalies in the ENSO run after removing the ENSO-related anomalies (Fig. 10d) resemble those in the no-ENSO run. The amplitude of precipitation anomalies (Fig. 10d) is comparable to that associated

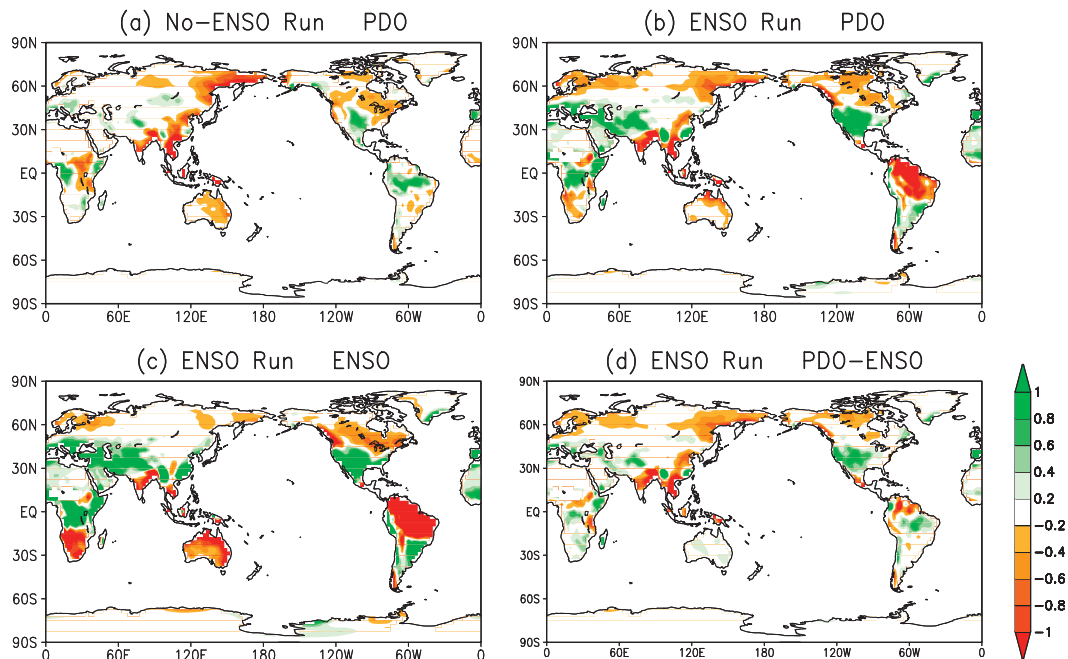


FIG. 10. As in Fig. 9, but for precipitation ($10^{-1} \text{ mm day}^{-1}$) over land.

with ENSO (Fig. 10c) over the Indian monsoon region but stronger over northeast Asia. Over the rest of the land areas, the PDO-related precipitation anomalies (Fig. 10d) are weaker than the ENSO response (Fig. 10c).

Composites for surface temperature anomalies at 2 m over land are shown in Fig. 11. In the no-ENSO run, the PDO-related 2-m temperature anomalies are limited to Asia, North America, and Greenland (Fig. 11a). Under the influence of ENSO, the PDO displays global-scale linkages with 2-m temperature anomalies (Fig. 11b). Similar to 200-hPa height and precipitation (Figs. 9b and 10b), the temperature anomalies (Fig. 11b) obtained from regressions against the PC time series of the PDO also contain the ENSO-induced anomalies (Fig. 11c). After removing the ENSO-related anomalies, the temperature anomalies associated with the PDO in the ENSO run (Fig. 11d) resemble those in the no-ENSO run (Fig. 11a), once again indicating a linear superposition of the ENSO- and PDO-related 2-m temperature patterns. Both precipitation and temperature anomaly patterns associated with the PDO (Figs. 10d and 11d) are consistent with the observations in North America (Mantua 1999; McCabe et al. 2004; Goodrich 2007) and the Indian monsoon region (Krishnan and Sugi 2003; Roy et al. 2003).

The above analysis indicates that the apparent global teleconnection of ENSO can be modulated by the PDO. The constructive or destructive interference between atmospheric and terrestrial anomalies due to ENSO can

be strengthened or weakened depending on the phase of the PDO (Gershunov and Barnett 1998; Yoon and Yeh 2010), and can have implications for seasonal prediction and attribution of seasonal climate anomalies (e.g., Gutzler et al. 2002).

6. Conclusions

We have investigated the influence of ENSO on PDV based on a comparison between the 500-yr NCEP CFS no-ENSO run and ENSO run. PDV in this study is represented by the two leading EOFs of monthly mean North Pacific SST anomalies. One is the PDO and another is the NPGO. In the no-ENSO run, the PDO is identified as EOF2 and the NPGO as EOF1. Compared to observations, PDV generated in the no-ENSO run displays relatively high frequencies at the decadal time scale and no strong signals at the interannual time scale. Under the influence of ENSO, the variability of the PDO is slightly increased and it appears as EOF1 in the ENSO run. ENSO not only enhances the PDO at the interannual time scale, but also shifts the PDO to a lower frequency at the decadal time scale with a spatial pattern closer to the observed. In contrast, the variability of the NPGO is weaker in the ENSO run than in the no-ENSO run.

We demonstrated that the PDO is more closely associated with the variability of the Aleutian low in the ENSO run than in the no-ENSO run. We also showed that ENSO modulates the variability of the Aleutian

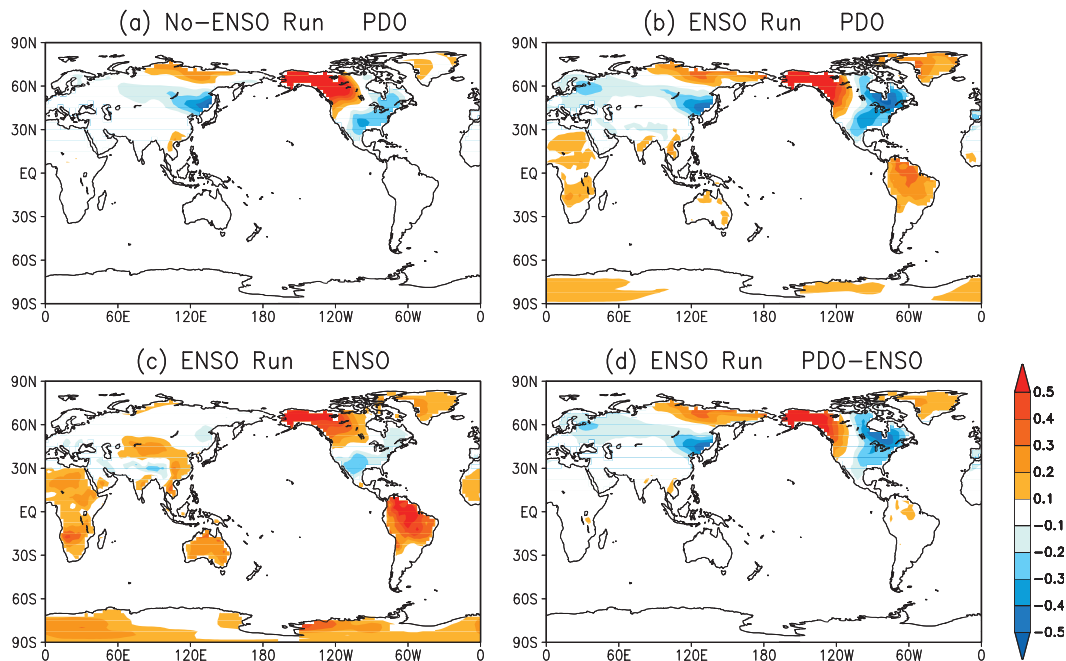


FIG. 11. As in Fig. 9, but for temperature (K) at 2 m over land.

low and increases the interannual variability of associated surface wind over the North Pacific. The anchoring provided by the slowly evolving and quasi-periodic forcing from ENSO drives North Pacific SST and results in a more persistent surface forcing for the PDO in the ENSO run than in the no-ENSO run. Alternatively, Wu and Liu (2003) suggested that tropical–extratropical atmospheric teleconnection may favor a particular type of wave motion in the North Pacific. The propagation of the oceanic waves may determine both spatial and temporal evolution of PDV. The variability of the PDO is also largely increased at the multidecadal time scales (~ 30 yr) in the ENSO run, and is associated with a deep structure in ocean temperature. However, the processes driving such changes in frequency of the PDO remain unclear, and will be investigated later.

Overall, the atmospheric anomalies associated with the PDO in the ENSO run—including 200-hPa height, precipitation, and 2-m temperature—are similar to those in the no-ENSO run after removing the ENSO-related components. This indicates a high degree of linearity in the interaction between ENSO-forced and the PDO-associated atmospheric anomaly patterns. In some regions, these precipitation and temperature anomalies are comparable to the ENSO signals, but in other regions they are weaker.

Given the influence of ENSO on the frequency and intensity of the PDO, the results presented in this study may have some implications of climate change. Although a consensus has not been reached on the changes

in ENSO in response to global warming (e.g., Latif and Keenlyside 2009; Collins et al. 2010), the regime shifts in ENSO have been detected in observations and in some model simulations for both present-day and future warming climate (Timmermann et al. 1999; Trenberth and Stepaniak 2001; Lin 2007). This may also imply some potential changes in the frequency of the PDO and the combined ENSO–PDO impacts.

The set of simulations without ENSO in the tropical Pacific clearly demonstrated the existence of the PDO as a mode of internal variability, which is consistent with the finding in Wu et al. (2003) that PDV can be generated through air–sea coupling within the North Pacific alone. Given that, in the context of ENSO’s global teleconnection, and its utility in skillful seasonal predictions, the superposition from the low-frequency component of the PDO may be an aspect to consider. Although the effect of ENSO on the temporal characteristics of the PDO is to generate a peak on the ENSO time scale (Fig. 2), and a particular phase of ENSO may induce a transition to a phase of the PDO consistent with ENSO, such transitions and the subsequent amplitude of the PDO may depend on the ambient low-frequency phase of the PDO, and may have implication for the predictability and attribution aspects of seasonal climate anomalies.

The analysis in this paper focused on documenting the influence of ENSO on the intrinsic variability of the PDO—an aspect that cannot be analyzed from the observational data. The analysis, however, did not focus

on the physical details of interactions between the ENSO-induced extratropical response and its influence on the characteristics of the PDO. This is at least one aspect that would be a logical extension of the present study for future work.

As mentioned previously, the PDO results from multiple mechanisms. In addition to the modulation of the surface wind, ENSO may also exert its influence on the PDO by altering other dynamical processes. For example, the PDO-related ocean temperature anomalies have different vertical scales between the no-ENSO run and ENSO run. It would be interesting to understand how the reemergence mechanism operates with and without ENSO. The generation of the PDO also involves zonal advection in the Kuroshio Extension and oceanic Rossby waves (Schneider and Cornuelle 2005). ENSO could also affect these oceanic processes and further the frequency and structure of the PDO. Therefore, more detailed diagnosis and in-depth comparisons will provide a better understanding of the physics responsible for the ENSO influence on the PDO, and will be reported later.

Acknowledgments. This work was supported by the NOAA Climate Test Bed (CTB) Program. We thank Michelle L'Heureux and Dr. Caihong Wen, three anonymous reviewers, and the editor for their insightful and constructive comments and suggestions.

REFERENCES

- Alexander, M. A., C. Deser, and M. S. Timlin, 1999: The re-emergence of SST anomalies in the North Pacific Ocean. *J. Climate*, **12**, 2419–2433.
- , I. Blade, M. Newman, J. R. Lanzante, N.-C. Lau, and J. D. Scott, 2002: The atmospheric bridge: The influence of ENSO teleconnections on the air–sea interaction over the global oceans. *J. Climate*, **15**, 2205–2231.
- An, S.-I., J.-S. Kug, A. Timmermann, I.-S. Kang, and O. Timm, 2007: The influence of ENSO on the generation of decadal variability in the North Pacific. *J. Climate*, **20**, 667–680.
- Behringer, D. W., and Y. Xue, 2004: Evaluation of the global ocean data assimilation system at NCEP: The Pacific Ocean. Preprints, *Eighth Symp. on Integrated Observing and Assimilation System for Atmosphere, Oceans, and Land Surface*, Seattle, WA, Amer. Meteor. Soc., 2.3. [Available online at http://ams.confex.com/ams/84Annual/techprogram/paper_70720.htm.]
- Ceballos, L. I., E. Di Lorenzo, C. D. Hoyos, N. Schneider, and B. Taguchi, 2009: North Pacific Gyre Oscillation synchronizes climate fluctuations in the eastern and western boundary systems. *J. Climate*, **22**, 5163–5174.
- Chhak, K. C., E. D. Lorenzo, N. Schneider, and P. F. Cummins, 2009: Forcing of low-frequency ocean variability in the northeast Pacific. *J. Climate*, **22**, 1255–1276.
- Collins, M., and Coauthors, 2010: The impact of global warming on the tropical Pacific Ocean and El Niño. *Nat. Geosci.*, **3**, 391–397.
- Deser, C., and Coauthors, 2012: ENSO and Pacific decadal variability in Community Climate System Model version 4. *J. Climate*, **25**, 2622–2651.
- Di Lorenzo, E., and Coauthors, 2008: North Pacific Gyre Oscillation links ocean climate and ecosystem change. *Geophys. Res. Lett.*, **35**, L08607, doi:10.1029/2007GL032838.
- , and Coauthors, 2009: Nutrient and salinity decadal variations in the central and eastern North Pacific. *Geophys. Res. Lett.*, **36**, L14601, doi:10.1029/2009GL038261.
- , K. M. Cobb, J. C. Furtado, N. Schneider, B. T. Anderson, A. Bracco, M. A. Alexander, and D. J. Vimont, 2010: Central Pacific El Niño and decadal climate change in the North Pacific. *Nat. Geosci.*, **3**, 762–765.
- Furtado, J. C., E. Di Lorenzo, N. Schneider, and N. A. Bond, 2011: North Pacific decadal variability and climate change in the IPCC AR4 models. *J. Climate*, **24**, 3049–3067.
- Gershunov, A., and T. P. Barnett, 1998: Interdecadal modulation of ENSO teleconnections. *Bull. Amer. Meteor. Soc.*, **79**, 2715–2725.
- Goodrich, G. B., 2007: Influence of the Pacific decadal oscillation on winter precipitation and drought during years of neutral ENSO in the western United States. *Wea. Forecasting*, **22**, 116–124.
- Gutzler, D. S., D. M. Kann, and C. Thornbrugh, 2002: Modulation of ENSO-based long-lead outlooks of southwestern U.S. winter precipitation by the Pacific decadal oscillation. *Wea. Forecasting*, **17**, 1163–1172.
- Kalnay, E., and Coauthors, 1996: The NCEP/NCAR 40-Year Reanalysis Project. *Bull. Amer. Meteor. Soc.*, **77**, 437–471.
- Kanamitsu, M., W. Ebisuzaki, J. Woollen, S.-K. Yang, J. J. Hnilo, M. Fiorino, and G. L. Potter, 2002: NCEP–DOE AMIP-II Reanalysis (R-2). *Bull. Amer. Meteor. Soc.*, **83**, 1631–1643.
- Kim, S. T., J.-Y. Yu, A. Kumar, and H. Wang, 2012: Examination of the two types of ENSO in the NCEP CFS model and its extratropical associations. *Mon. Wea. Rev.*, **140**, 1908–1923.
- Krishnan, R., and M. Sugi, 2003: Pacific decadal oscillation and variability of the Indian summer monsoon rainfall. *Climate Dyn.*, **21**, 233–242.
- Latif, M., and T. P. Barnett, 1994: Causes of decadal climate variability over the North Pacific and North America. *Science*, **266**, 634–637.
- , and N. S. Keenlyside, 2009: El Niño/Southern Oscillation response to global warming. *Proc. Natl. Acad. Sci. USA*, **106**, 20 578–20 583.
- Lin, J.-L., 2007: Interdecadal variability of ENSO in 21 IPCC AR4 coupled GCMs. *Geophys. Res. Lett.*, **34**, L12702, doi:10.1029/2006GL028937.
- Liu, Z., 2012: Dynamics of interdecadal climate variability: A historical perspective. *J. Climate*, **25**, 1963–1995.
- Mantua, N. J., 1999: The Pacific decadal oscillation and climate forecasting for North America. *Climate Risk Solutions*, **1**, 10–13.
- , S. R. Hare, Y. Zhang, J. M. Wallace, and R. Francis, 1997: A Pacific interdecadal climate oscillation with impacts on salmon production. *Bull. Amer. Meteor. Soc.*, **78**, 1069–1079.
- McCabe, G. J., M. A. Palecki, and J. L. Betancourt, 2004: Pacific and Atlantic Ocean influences on multidecadal drought frequency in the United States. *Proc. Natl. Acad. Sci. USA*, **101**, 4136–4141.
- Moorthi, S., H.-L. Pan, and P. Caplan, 2001: Changes to the 2001 NCEP operational MRF/AVN global analysis/forecast system. NWS Tech. Procedures Bulletin 484, 14 pp. [Available online at <http://www.nws.noaa.gov/om/tpb/484.htm>.]

- Newman, M., G. P. Compo, and M. A. Alexander, 2003: ENSO-forced variability of the Pacific decadal oscillation. *J. Climate*, **16**, 3853–3857.
- Pacanowski, R. C., and S. M. Griffies, 1998: MOM 3.0 manual. NOAA/Geophysical Fluid Dynamics Laboratory, 668 pp.
- Pan, H.-L., and L. Mahrt, 1987: Interaction between soil hydrology and boundary layer developments. *Bound.-Layer Meteor.*, **38**, 185–202.
- Qiu, B., 2003: Kuroshio Extension variability and forcing of the Pacific decadal oscillation: Responses and potential feedback. *J. Phys. Oceanogr.*, **33**, 2465–2482.
- Reynolds, R. W., N. A. Rayner, T. M. Smith, D. C. Stokes, and W. Wang, 2002: An improved in situ and satellite SST analysis for climate. *J. Climate*, **15**, 1609–1625.
- Rogers, J. C., 1981: The North Pacific Oscillation. *J. Climatol.*, **1**, 39–58.
- Roy, S. S., G. B. Goodrich, and R. C. Balling Jr., 2003: Influence of El Niño/Southern Oscillation, Pacific decadal oscillation, and local sea surface temperature anomalies on peak season monsoon precipitation in India. *Climate Res.*, **25**, 171–178.
- Saha, S., and Coauthors, 2006: The NCEP Climate Forecast System. *J. Climate*, **19**, 3483–3517.
- Schneider, N., and B. D. Cornuelle, 2005: The forcing of the Pacific decadal oscillation. *J. Climate*, **18**, 4355–4373.
- Shakun, J., and J. Shaman, 2009: Tropical origins of North and South Pacific decadal variability. *Geophys. Res. Lett.*, **36**, L19711, doi:10.1029/2009GL040313.
- Smith, T. M., R. W. Reynolds, T. C. Peterson, and J. Lawrimore, 2008: Improvements to NOAA's historical merged land-ocean surface temperature analysis (1880–2006). *J. Climate*, **21**, 2283–2296.
- Taguchi, B., S.-P. Xie, N. Schneider, M. Nonaka, H. Sasaki, and Y. Sasai, 2007: Decadal variability of the Kuroshio Extension: Observations and an eddy-resolving model hindcast. *J. Climate*, **20**, 2357–2377.
- Timmermann, A., J. Oberhuber, A. Bacher, M. Esch, M. Latif, and E. Roeckner, 1999: Increased El Niño frequency in a climate model forced by future greenhouse warming. *Nature*, **398**, 694–696.
- Trenberth, K. E., and D. P. Stepaniak, 2001: Indices of El Niño evolution. *J. Climate*, **14**, 1697–1701.
- Vecchi, G. A., M. Zhao, H. Wang, G. Villarini, A. Rosati, A. Kumar, I. M. Held, and R. Gudgel, 2011: Statistical-dynamical predictions of seasonal North Atlantic hurricane activity. *Mon. Wea. Rev.*, **139**, 1070–1082.
- Wallace, J. M., and D. S. Gutzler, 1981: Teleconnections in the geopotential height field during the Northern Hemisphere winter. *Mon. Wea. Rev.*, **109**, 784–812.
- Wang, B., and Coauthors, 2008: How accurately do coupled climate models predict the Asian-Australian monsoon interannual variability? *Climate Dyn.*, **30**, 605–619.
- Wang, H., J.-K. E. Schemm, A. Kumar, W. Wang, L. Long, M. Chelliah, G. D. Bell, and P. Peng, 2009: A statistical forecast model for Atlantic seasonal hurricane activity based on the NCEP dynamical seasonal forecast. *J. Climate*, **22**, 4481–4500.
- , A. Kumar, W. Wang, and Y. Xue, 2012: Seasonality of the Pacific decadal oscillation. *J. Climate*, **25**, 25–38.
- Wang, W., S. Saha, H.-L. Pan, S. Nadiga, and G. White, 2005: Simulation of ENSO in the new NCEP Coupled Forecast System Model (CFS03). *Mon. Wea. Rev.*, **133**, 1574–1593.
- , M. Chen, and A. Kumar, 2010: An assessment of the CFS real-time seasonal forecasts. *Wea. Forecasting*, **25**, 950–969.
- Wu, L., and Z. Liu, 2003: Decadal variability in the North Pacific: The eastern North Pacific mode. *J. Climate*, **16**, 3111–3131.
- , —, R. Gallimore, R. Jacob, D. Lee, and Y. Zhong, 2003: Pacific decadal variability: The tropical Pacific mode and the North Pacific mode. *J. Climate*, **16**, 1101–1120.
- Yang, S., Y. Jiang, D. Zheng, R. W. Higgins, Q. Zhang, V. E. Kousky, and M. Wen, 2009: Variations of U.S. regional precipitation and simulations by the NCEP CFS: Focus on the Southwest. *J. Climate*, **22**, 3211–3231.
- Yeh, S.-W., and B. P. Kirtman, 2005: Pacific decadal variability and decadal ENSO amplitude modulation. *Geophys. Res. Lett.*, **32**, L05703, doi:10.1029/2004GL021731.
- Yoon, J., and S.-W. Yeh, 2010: Influence of the Pacific decadal oscillation on the relationship between El Niño and the northeast Asian summer monsoon. *J. Climate*, **23**, 4525–4537.
- Zhang, Q., A. Kumar, Y. Xue, W. Wang, and F.-F. Jin, 2007: Analysis of the ENSO cycle in the NCEP coupled forecast model. *J. Climate*, **20**, 1265–1284.
- Zhang, Y., J. M. Wallace, and D. S. Battisti, 1997: ENSO-like interdecadal variability. *J. Climate*, **10**, 1004–1020.